small structures
www.small-structures.com

Experimental and Computational Insights into the Structural Dynamics of the Fc Fragment of IgG1 Subtype from Biosimilar VEGF-Trap

*Ebru Destan, Engin Turkut, Alper Aldeniz, Jungmin Kang, Takehiko Tosha, Makina Yabashi, Baris Yilmaz, Ahmet Can Timucin, Hiroaki Matsuura, Yoshiaki Kawano, Irfan Cinkaya, and Hasan DeMirci**

The constant fragment (Fc) of the immunoglobulin G1 (IgG1) subtype is increasingly recognized as a crucial scaffold in the development of advanced therapeutics due to its enhanced specificity, efficacy, and extended half-life. A prime example is VEGF-Trap (Aflibercept), a recombinant fusion protein that merges the Fc region of the IgG1 subtype with the binding domains of vascular endothelial growth factor receptors (VEGFR)-1 and VEGFR-2. The Fc region's role in N-glycosylation is particularly important, as it significantly influences protein stability. Herein, the first near-physiological temperature structures of the N-glycan-bound Fc fragment of IgG1 subtype from a biosimilar VEGF-Trap are presented, determined using the SPring-8 Angstrom Compact free electron LAser (SACLA) and the Turkish Light Source (Turkish DeLight). Comparative analysis with cryogenic structures, including existing data, reveals alternate conformations within the glycan-binding pocket. Furthermore, molecular dynamics simulations indicate the presence of a high degree of structural plasticity, explaining how the protein adapts its structure through conformational changes. The observed structural fluctuations/conformational changes demonstrate the effect of N-glycans on protein stability. These findings offer new insights into the molecular basis of Fc-mediated functions and provide valuable information for the design of next-generation therapeutics.

1. Introduction

Biology involves a myriad of highly dynamic processes, and a comprehensive understanding of the structural dynamics occurring at the atomic level and near-physiological conditions is a necessity and still remains a significant challenge. X-Ray crystallography is a very robust and powerful technique, allowing the determination of the arrangement of atoms in a crystal to reveal the 3D structures of biological macromolecules.[1] Recent developments of X-Ray free electron lasers (XFELs) and sample delivery methods have expanded the boundaries in structural biology.[2–5] These advancements provided new insight into the treatment of diseases in medicine. Here, the information obtained from high-resolution structures of biomolecules can be used in drug design studies, leading to a better understanding of the action mechanism for a potential treatment.[6,7]

E. Destan, H. DeMirci
Department of Molecular Biology and Genetics
Koc University
34450 Istanbul, Türkiye
E-mail: hdemirci@ku.edu.tr

E. Turkut, A. Aldeniz, B. Yilmaz, I. Cinkaya
Biotechnology
DEVA Holding AS
59510 Tekirdag, Türkiye

J. Kang, T. Tosha, M. Yabashi, H. Matsuura, Y. Kawano
RIKEN SPring-8 Center
1-1-1 Kouto, Sayo-cho, Sayo-gun, Hyogo 679-5148, Japan

The ORCID identification number(s) for the author(s) of this article can be found under https://doi.org/10.1002/sstr.202400680.

© 2025 The Author(s). Small Structures published by Wiley-VCH GmbH. This is an open access article under the terms of the Creative Commons Attribution License, which permits use, distribution and reproduction in any medium, provided the original work is properly cited.

DOI: 10.1002/sstr.202400680

T. Tosha, H. Matsuura
Graduate School of Science
University of Hyogo
3-2-1 Kouto, Kamigori-cho, Ako-gun, Hyogo 678-1297, Japan

M. Yabashi
Japan Synchrotron Radiation Research Institute (JASRI)
1-1-1 Kouto, Sayo-cho, Sayo-gun, Hyogo 679-5198, Japan

A. Can Timucin
Department of Molecular Biology and Genetics
Acibadem University
34752 Istanbul, Türkiye

H. DeMirci
Stanford PULSE Institute
SLAC National Laboratory
Menlo Park, CA 94025, USA

H. DeMirci
Koc University Isbank Center for Infectious Diseases (KUISCID)
Koc University
34010 Istanbul, Türkiye

Since the first discovery of immunoglobulin-like protein by Bence Jones in 1845, the complex nature of immunoglobulins continues to unveil new frontiers in science.[8] Immunoglobulins, known as antibodies, are glycoproteins produced primarily by B cells in the adaptive immune system.[9] These Y-shaped proteins play a pivotal role in the immune defense mechanism, specifically by recognizing, binding to foreign substances/molecules, and neutralizing them or targeting them for destruction. An immunoglobulin involves the attachment of antigen-binding fragment (Fab) and constant fragment (Fc) through the hinge region.[10] The polypeptide chains are known as heavy and light chains composed of variable (V) and constant (C) regions.[11] While the V region contributes to the antigen-binding site, the C region determines the isotype. The exons encoding the V regions are known as V, D (diversity), or J (joining) genes. The random recombination of the V(D)J gene is the key mechanism to produce antibody diversity.[12] Furthermore, somatic hypermutation introduces additional diversity by inducing random mutations in the antibody genes, leading to subtle changes in the antibody's specificity.[13] There are five isotypes of immunoglobulins (Ig): IgA, IgD, IgE, IgG, and IgM. Among them, IgG (specifically the IgG1 subtype) is the most abundant Ig isotype within the blood with its extremely long serum half-life. This makes IgG a suitable scaffold for the design of novel therapeutics.[14,15]

Wet age-related macular degeneration (AMD) is a disease caused by the formation of new anomalous blood vessels driven by angiogenesis in the retina through choroidal neovascularization (CNV).[16] As vascular endothelial growth factor (VEGF), proangiogenic cytokines, have a vital role in the progression of angiogenesis, the antiangiogenic agents that target it have been designed.[17,18] VEGF-Trap is a recombinant fusion protein that was first approved by the US Federal Drug Administration (FDA) for the treatment of wet AMD on 18 November 2011.[19,20] Its dimeric structure is composed of two chains, the binding domains of vascular endothelial growth factor receptor (VEGFR)-1(Ig2 region) and VEGFR-2(Ig3 region) fused with the Fc fragment of IgG1 subtype (Figure S1a, Supporting Information).

The Fc fragment of the IgG1 subtype mediates effector functions of the immune system including Fc receptor binding, antibody-dependent cellular cytotoxicity (ADCC), antibody-dependent cellular phagocytosis (ADCP), and structure stability.[21] Compared to all subtypes (IgG1, IgG2, IgG3, and IgG4), IgG1 has the highest affinity to Fcγ receptor (FcγR).[22] Additionally, the Fc fragment contributes to extended drug half-life, improving drug availability and patient compliance. Its capacity for immunomodulation, achieved through interactions with FcγR on immune cells, is particularly valuable in drug development for autoimmune diseases.[23,24] Moreover, N-glycosylation in the Fc fragment is a pivotal post-translational modification that significantly influences the diversification of antibody function.[25] The addition of glycans to the Fc fragment contributes to the interaction with FcγR.[26,27] Mature Fc glycoforms are N-linked and involve seven saccharides: 4 N-acetylglucosamine (GlcNAc) and 3 mannose (Man) residues (Figure S1b, Supporting Information). The core glycans can be modified further by the addition of sugars including core fucose (Fuc), bisecting GlcNAc, galactose (Gal) at one or both arms, and in the presence of galactose, N-acetylneuraminic acid (NeuAc) or sialic acid.[28]

In this study, we revealed four crystal structures of the Fc fragment of IgG1 subtype from biosimilar VEGF-Trap by using three different X-Ray sources: Home X-Ray source diffractometer (XRD) (Turkish Light Source (Turkish DeLight)), Synchrotron (Super Photon ring-8 GeV (SPring-8)), and XFEL (SPring-8 Angstrom Compact free electron LAser (SACLA)). Rigaku Oxford Diffraction XtaLAB Synergy-S diffractometer equipped with XtalCheck-S plate reader system provides rapid and high-quality data collection from protein crystals at ambient temperature (Figure S2a, Supporting Information). Serially collected diffraction data from low-cost 72-well Terasaki crystallization plates using a multiwell-multicrystal plate reader with less amount of crystals offers a cheaper and readily available alternative in-house method to serial femtosecond X-Ray crystallography (SFX) techniques performed at XFELs.[29] The advent of bright X-Ray sources such as synchrotron and XFEL facilities has unveiled challenges in protein crystallography, notably pertaining to radiation-induced damage incurred during X-Ray irradiation.[30] The SPring-8/SACLA experimental facility in Japan enables users to perform macromolecular X-Ray crystallography experiments with powerful X-rays. The beamline BL32XU with the goniometer-based fully automated data collection system at the SPring-8 synchrotron radiation facility provides high-throughput diffraction data at cryogenic temperature.[31,32] Although cryogenic data collection is a commonly used approach for limiting radiation damage, freezing of a crystal can perturb crystal lattice and protein structures.[33,34] A near-physiological crystallographic method that provides high spatial resolution data free of radiation damage and consumes less crystal has been desired. Here, SFX represents an important advancement in protein crystallography as it allows data collection at ambient temperature from a crystal slurry and mitigates radiation damage through the use of ultrashort femtosecond and ultrabright X-Ray pulses.[2,35] SACLA Beamline 2 experimental station has a measurement system with a 10 fs pulse duration and 30 Hz or 60 Hz pulse repetition rate depending on the operation mode, which consists of components including the sample chamber, injector, detector, and data acquisition system.[36] For the sample delivery, highly viscous carriers have a great advantage compared to liquid-jet injectors as the sample consumption can be reduced by lowering the flow rate (Figure S2b,c, Supporting Information). The high-viscosity cartridge-type (HVC) injector has been designed for SFX experiments equipped in the Diverse Application Platform for Hard X-Ray Diffraction in SACLA (DAPHNIS).[4,37]

Together with highlighting the structural dynamics of the Fc fragment of the IgG1 subtype, this study provides an invaluable opportunity to compare the abilities of these X-Ray sources. In addition to X-Ray crystallography experiments, molecular dynamics (MD) simulations were performed to reveal the detailed interaction mechanism of N-glycans with the Fc fragment of the IgG1 subtype. The findings of this study hold the promise of paving the way for designing novel therapeutics with enhanced efficacy.

2. Results and Discussion

2.1. Near-Physiological-Temperature Structures Reveal Conformational Flexibility Occurring Through N-Glycosylation

We determined two ambient temperature crystal structures of the Fc fragment of the IgG1 subtype from the biosimilar

© 2025 The Author(s). Small Structures published by Wiley-VCH GmbH

26884062, 2025, 8, Downloaded from https://onlinelibrary.wiley.com/doi/10.1002/sstr.202400680 by Koc University, Wiley Online Library on [19/08/2025]. See the Terms and Conditions (https://onlinelibrary.wiley.com/terms-and-conditions) on Wiley Online Library for rules of use; OA articles are governed by the applicable Creative Commons License

VEGF-Trap molecule by using two different X-Ray sources. Both radiation damage-free XFEL SFX Fc^{SFX} and in-house XRD $Fc^{XRD(Ambient)}$ crystal structures were obtained in orthorhombic crystal form, $P2_12_12_1$ space group at 2.00 Å and 2.60 Å resolutions, respectively (**Figure 1**a,b and Table S1, Supporting Information). The well-defined electron density map was observed in the N-glycosylation region where N-glycans bound to Fc fragment of IgG1 subtype: G1F* (chain A) and G0F-GlcNAc (chain B) (GlyTouCan IDs: G56907CZ & G45889JQ) (Figure S3, Supporting Information). Moreover, the glycan profile that binds to the T32 site (N_{282}) was revealed by using mass spectrometry (MS) (Figure S4, Supporting Information). Based on the MS data, G1F* was observed with higher intensity compared to G0F-GlcNAc. The glycan-binding pocket of two ambient temperature Fc^{SFX} and $Fc^{XRD(Ambient)}$ structures is analyzed to reveal the structural details of the N-glycosylation process (**Figure 2**a,b). In

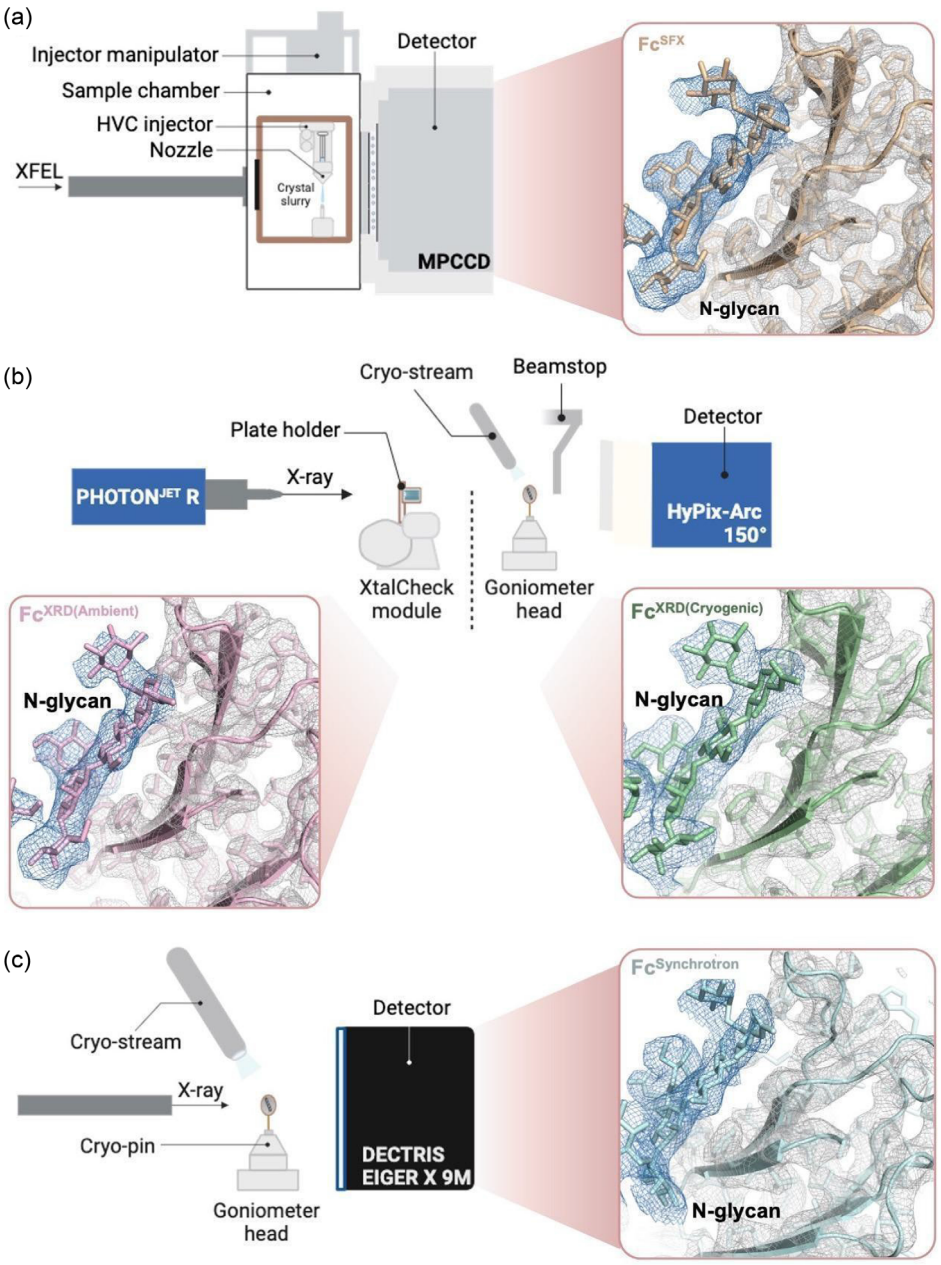


Figure 1. Crystal structures of Fc fragments of IgG1 subtype from biosimilar VEGF-Trap fusion protein. a) The 2.0 Å crystal structure of the Fc fragment (Fc^{SFX}) at ambient temperature is obtained by the SFX technique at SACLA. b) The 2.6 Å crystal structure of the Fc fragment ($Fc^{XRD(Ambient)}$) at ambient temperature is obtained from Turkish DeLight while the 3.14 Å crystal structure ($Fc^{XRD(Cryogenic)}$) was obtained at cryogenic temperature. c) The 2.64 Å crystal structure of the Fc fragment ($Fc^{Synchrotron}$) at cryogenic temperature is obtained at Spring-8. The 2Fo-Fc electron densities are contoured at 1 σ level and colored in sky blue (N-glycans) and gray. Fc^{SFX}, $Fc^{XRD(Ambient)}$, $Fc^{Synchrotron}$, and $Fc^{XRD(Cryogenic)}$ structures are colored wheat, light pink, pale cyan, and pale green, respectively. PDB IDs and GlyTouCan IDs are indicated in Table S2, Supporting Information.

© 2025 The Author(s). Small Structures published by Wiley-VCH GmbH

26884062, 2025, 8, Downloaded from https://onlinelibrary.wiley.com/doi/10.1002/sstr.202400680 by Koc University, Wiley Online Library on [19/08/2025]. See the Terms and Conditions (https://onlinelibrary.wiley.com/terms-and-conditions) on Wiley Online Library for rules of use; OA articles are governed by the applicable Creative Commons License

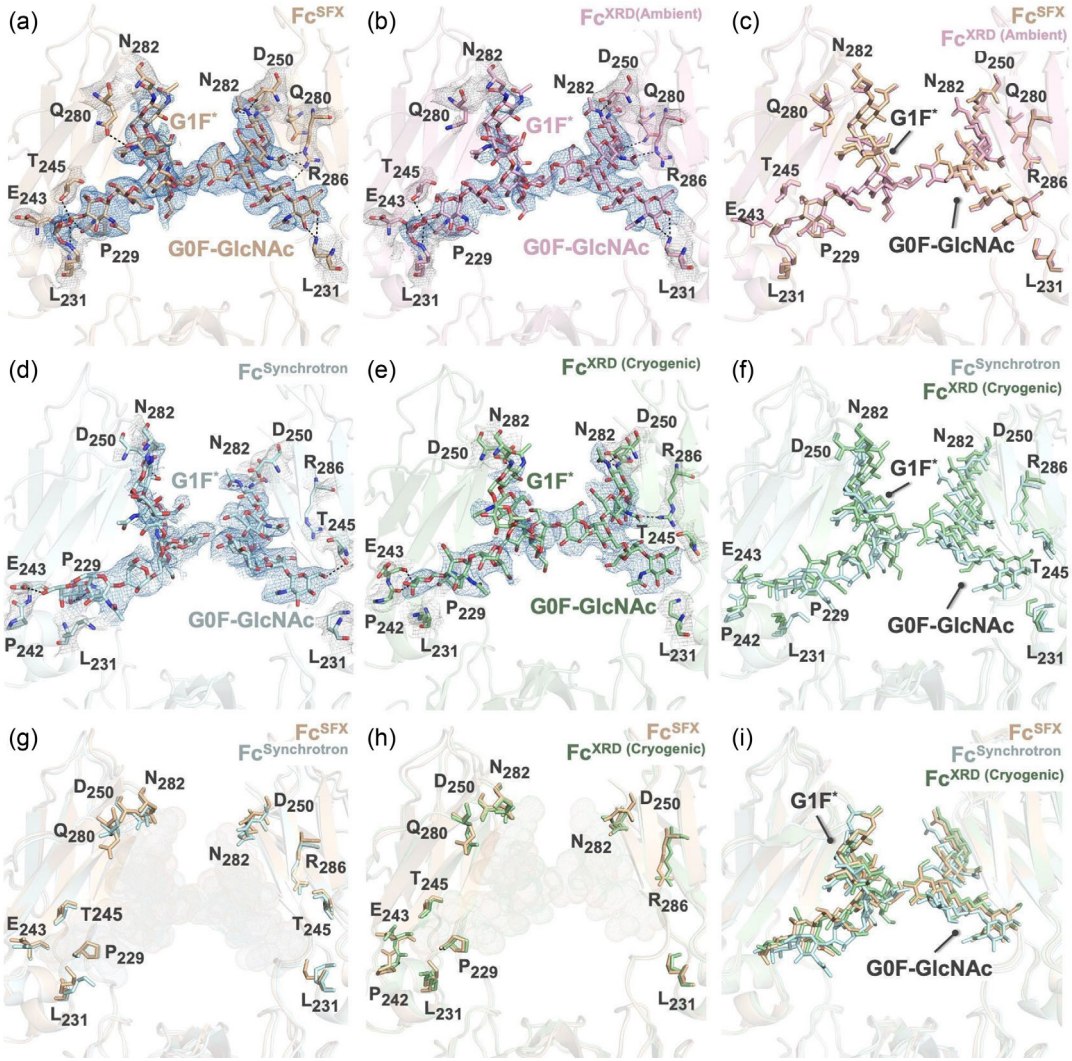


Figure 2. The representation of glycan-binding sites. a,b) Glycan-binding sites for the Fc^{SFX} and $Fc^{XRD(Ambient)}$ structures are represented to detect the conformational changes between two ambient temperature structures. c) Fc^{SFX} and $Fc^{XRD(Ambient)}$ structures are superposed with an RMSD value of 0.144 Å. d,e) Glycan-binding sites for the $Fc^{Synchrotron}$ and $Fc^{XRD(Cryogenic)}$ structures are represented to detect the conformational changes between ambient and cryogenic temperature structures. f) Fc^{SFX} and $Fc^{XRD(Ambient)}$ structures are superposed with an RMSD value of 0.789 Å. g–i) Glycan-binding sites for ambient and cryogenic temperature structures are compared to detect the conformational changes. Fc^{SFX} and $Fc^{Synchrotron}$ structures are superposed with an RMSD value of 0.672 Å while Fc^{SFX} and $Fc^{XRD(Cryogenic)}$ structures are superposed with an RMSD value of 0.433 Å. Polar contacts are shown with black dashed lines. The 2Fo-Fc electron densities are contoured at 1 σ level and colored in sky blue (N-glycans) and gray (protein residues). Fc^{SFX}, $Fc^{XRD(Ambient)}$, $Fc^{Synchrotron}$, and $Fc^{XRD(Cryogenic)}$ structures are colored wheat, light pink, pale cyan, and pale green, respectively. PDB IDs and GlyTouCan IDs are indicated in Table S2, Supporting Information.

comparison, better electron density was observed for the Fc^{SFX} structure at 2.00 Å resolution. G1F* was detected to be more weakly bound to chain A of the Fc fragment in both structures compared to G0F-GlcNAc which binds to chain B. This result suggests that the chains of the homodimer Fc fragment are affected differently by the binding of N-glycans, indicating the importance of N-glycan composition on protein stability. To further investigate the structural dynamics, flexible regions were determined through b-factor analysis (**Figure 3** and S5, Supporting Information). Chain A is observed as more flexible compared to chain B, leading to the less-defined electron density for G1F*. The comparison of ambient temperature Fc^{SFX} and $Fc^{XRD(Ambient)}$ structures with a previously published $Fc^{G0\&G0F}$ structure indicated that loop regions near the glycan-binding site are highly flexible while the core region maintains its stability. Although N-glycosylation is known for increased protein stability, there are cases where N-glycosylation causes flexibility in the structure by inducing altered conformations.[38–40] Based on the $Fc^{Deglycosylated}$ structure, the binding of the glycan causes backbone displacements, inducing changes in protein thermal stability. An important entropic contribution comes from the flexibility of the loop conformation in the glycan-bound state (Figure S6, Supporting Information).

© 2025 The Author(s). Small Structures published by Wiley-VCH GmbH

26884062, 2025, 8, Downloaded from https://onlinelibrary.wiley.com/doi/10.1002/sstr.202400680 by Koc University, Wiley Online Library on [19/08/2025]. See the Terms and Conditions (https://onlinelibrary.wiley.com/terms-and-conditions) on Wiley Online Library for rules of use; OA articles are governed by the applicable Creative Commons License

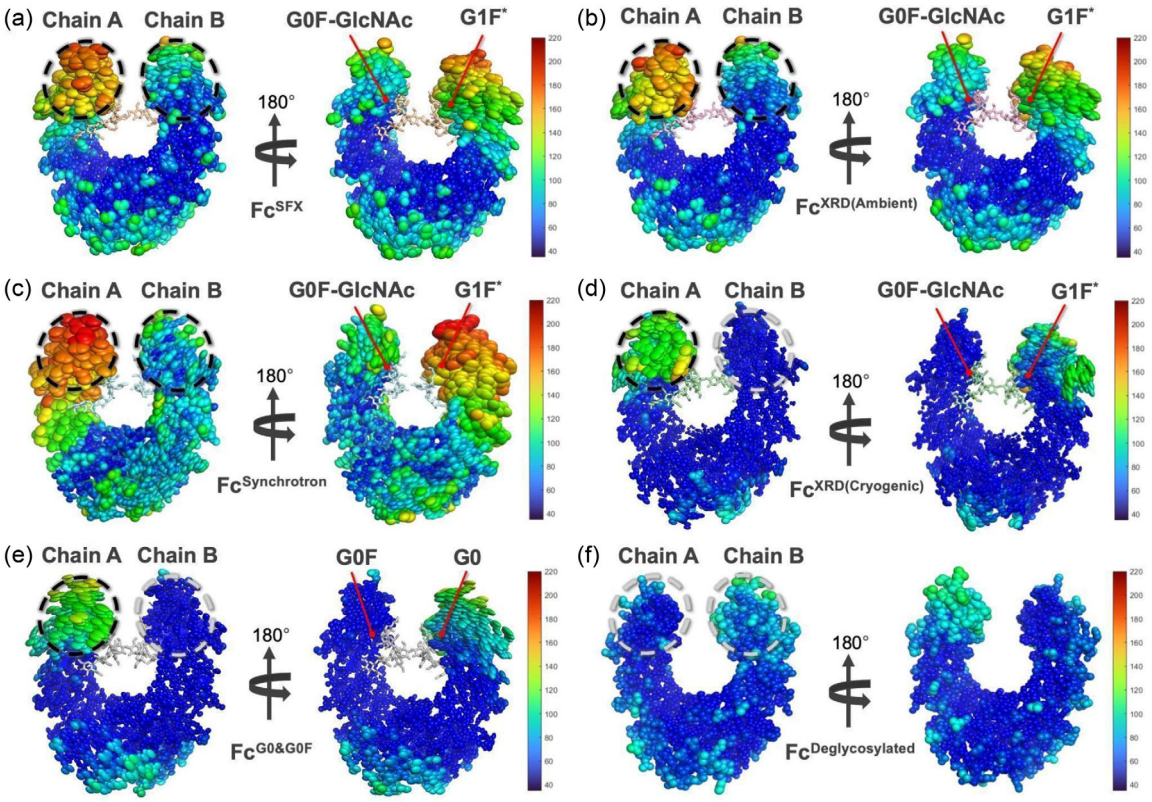


Figure 3. Ellipsoid representation of the crystal structures of the Fc fragment of IgG1 subtype. a,b) Ambient temperature Fc^{SFX} and $Fc^{XRD(Ambient)}$ structures are visualized with ellipsoid representation and colored based on *b*-factors (spectrum: range (35.00000–220.00000)). c,d) Cryogenic temperature $Fc^{Synchrotron}$ and $Fc^{XRD(Cryogenic)}$ structures are visualized with ellipsoid representation and colored based on *b*-factors (spectrum: range (35.00000–220.00000)). e,f) Previously available $Fc^{G0\&G0F}$ and $Fc^{Deglycosylated}$ structures (PDB IDs: 4W4N&7RHO, respectively) are visualized with ellipsoid representation and colored based on *b*-factors (spectrum: range (35.00000–220.00000)). Ellipsoid representation is used to indicate the flexibility of the macromolecules. Highly flexible regions around the glycan-binding pocket are indicated by dashed black circles. If these regions are detected as more stable compared to other structures, dashed circles are colored gray. RABDAM analysis for Fc^{SFX}, $Fc^{XRD(Ambient)}$, $Fc^{Synchrotron}$, and $Fc^{XRD(Cryogenic)}$ structures are summarized in Figure S10, Supporting Information. PDB IDs and GlyTouCan IDs are indicated in Table S2, Supporting Information.

Two ambient temperature Fc^{SFX} and $Fc^{XRD(Ambient)}$ structures were superposed with the root-mean-square displacement (RMSD) value 0.144 Å and only minor conformational changes were observed between the two structures, suggesting that the Rigaku XRD offers high-quality data collection at ambient temperature (Figure 2c and S7a,c, Supporting Information). In the Fc^{SFX} structure, N-glycans interact with P_{229}, L_{231}, E_{243}, T_{245}, Q_{280}, and N_{282} residues of chain A and L_{231}, D_{250}, N_{282}, and R_{286} residues of chain B. For the $Fc^{XRD(Ambient)}$ structure, the same polar contacts are observed except the interaction with Q_{280} residue was observed between G0F-GlcNAc rather than G1F*. Furthermore, it is observed that the number of water molecules (Wat) around the glycan-binding site differs between Fc^{SFX} and $Fc^{XRD(Ambient)}$ structures (Figure S8, Supporting Information). The conserved hydrogen binding network may play a key role during the binding of N-glycans.[41] Wat_5, Wat_{111}, and Wat_{126} for Fc^{SFX} structure and Wat_8, Wat_{62}, and Wat_{119} for $Fc^{XRD(Ambient)}$ were observed as conserved and performed hydrogen bond interaction with the critical residues during the interaction with N-glycans. The same conserved water molecule (Wat_{702}) was observed for long-chain N-glycan (G1F) in the previously published structure (PDB ID: 5VGP)($Fc^{G1F\&G0F}$). To detect the alternate conformations, the Fc^{SFX} and $Fc^{XRD(Ambient)}$ structures are superposed with previously published structures (**Figure 4** and S9, Supporting Information). While only minor conformation changes were observed in the active site residues for the $Fc^{G0\&G0F}$ structure, major conformational changes were observed for $Fc^{G1F*-GlcNAc}$ (PDB ID: 1H3V) and $Fc^{G1F\&G0F}$ structures (**Figure 5** and S10a,b, Supporting Information). Especially, significant conformational changes were observed on L_{231}, T_{245}, D_{250}, Q_{280}, N_{282}, and R_{286} residues, indicating the influence of N-glycan composition on the protein. The comparison of glycan-binding pockets for long and short-chain glycans revealed a significant shift in the position of N-glycans and alternate conformations for the sugar molecules which are the building blocks of N-glycans.

2.2. Alternate Conformations are Observed in the Cryogenic-Temperature Structures

$Fc^{Synchrotron}$ and $Fc^{XRD(Cryogenic)}$ structures were determined at 2.64 and 3.14 Å resolutions from different X-Ray sources in orthorhombic crystal form, $P2_12_12_1$ space group at cryogenic temperature (Figure 1b,c and Table S1, Supporting Information). Here,

© 2025 The Author(s). Small Structures published by Wiley-VCH GmbH

26884062, 2025, 8, Downloaded from https://onlinelibrary.wiley.com/doi/10.1002/sstr.202400680 by Koc University, Wiley Online Library on [19/08/2025]. See the Terms and Conditions (https://onlinelibrary.wiley.com/terms-and-conditions) on Wiley Online Library for rules of use; OA articles are governed by the applicable Creative Commons License

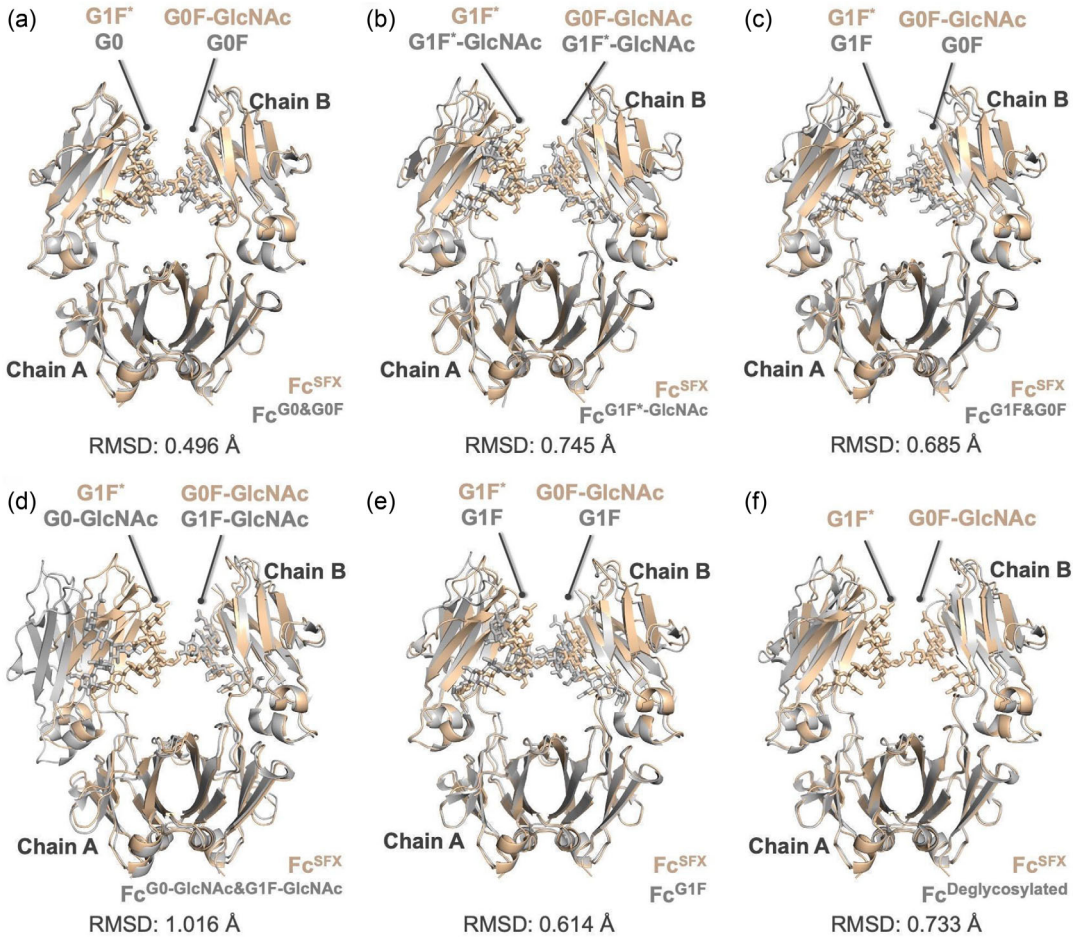


Figure 4. Conformational changes between Fc^{SFX} and cryogenic temperature structures of Fc fragment of IgG1 subtype. a–f) Fc^{SFX} structure is superposed with previously published cryogenic temperature structures of the Fc fragment of the IgG1 subtype (PDB IDs: 4W4N ($Fc^{G0\&G0F}$), 1H3V ($Fc^{G1F*-GlcNAc}$), 5VGP ($Fc^{G1F\&G0F}$), 5JII ($Fc^{G0-GlcNAc\&G1F-GlcNAc}$), 7LBL ($Fc^{G1F}$), and 7RHO ($Fc^{Deglycosylated}$)). Fc^{SFX} structure is colored in wheat while superposed structures are colored in gray. PDB IDs and GlyTouCan IDs are indicated in Table S2, Supporting Information.

the difference between the data from multiple crystals and a single crystal impacted the overall structural dynamics. The data statistics indicated that cryogenic temperature structures have slightly higher R_{work}/R_{free} values with relatively lower resolution compared to ambient temperature structures. This may originate from the impact of cryo-freezing which is one of the challenges of cryogenic temperature data collection.[42] To reveal the structural dynamics, $Fc^{Synchrotron}$ and $Fc^{XRD(Cryogenic)}$ structures were analyzed based on the defined electron density maps. Commonly, both cryogenic temperature structures displayed significant conformational changes in the glycan-binding site, highlighting the importance of structural dynamics at near-physiological temperatures (Figure 2 and S11, Supporting Information). Previously observed common hydrogen bond interactions between the N-glycans and L_{231} (chain A & B), T_{245} (chain A), D_{250} (chain B), and R_{286} (chain B) residues were not observed for the $Fc^{Synchrotron}$ structure. The major conformational changes were observed on the L_{231} and Q_{280} (weak electron density for $Fc^{Synchrotron}$ structure) residues in the chain A while L_{231}, D_{250}, and N_{282} in the chain B (Figure 2g). For the $Fc^{XRD(Cryogenic)}$ structure, G1F* interacts with P_{229}, P_{242}, E_{243}, D_{250}, and N_{282} residues of chain A while G0F-GlcNAc interacts with D_{250}, R_{286}, and N_{282} residues of chain B. The major conformational changes were observed on the L_{231}, P_{242}, E_{243}, and Q_{280} (weak electron density for $Fc^{XRD(Cryogenic)}$ structure) residues in chain A while L_{231} and R_{286} in chain B (Figure 2h). Interestingly, the comparison of glycan-binding positions indicated the altered N-glycan confirmation for cryogenic structures, especially the $Fc^{Synchrotron}$ structure (Figure 2i). These findings indicate the altered conformational state of the N-glycan-bound Fc fragment of IgG1 subtype at cryogenic temperature. Similar to the ambient temperature structures, less-defined electron density was observed for G1F*, which binds to the relatively more flexible chain A compared to the G0F-GlcNAc-bound chain B (Figure 3 and S3, Supporting Information). To highlight the details of structural dynamics and elucidate the radiation damage from different X-Ray sources, b-factors were analyzed by using RABDAM software (Figure 3 and S12, Supporting Information).[43] RABDAM generates the B_{Damage} metric using atomic isotropic *B*-factor values in environments with similar packing density, and the B_{net} metric, which is a derivative of

© 2025 The Author(s). Small Structures published by Wiley-VCH GmbH

26884062, 2025, 8, Downloaded from https://onlinelibrary.wiley.com/doi/10.1002/sstr.202400680 by Koc University, Wiley Online Library on [19/08/2025]. See the Terms and Conditions (https://onlinelibrary.wiley.com/terms-and-conditions) on Wiley Online Library for rules of use; OA articles are governed by the applicable Creative Commons License

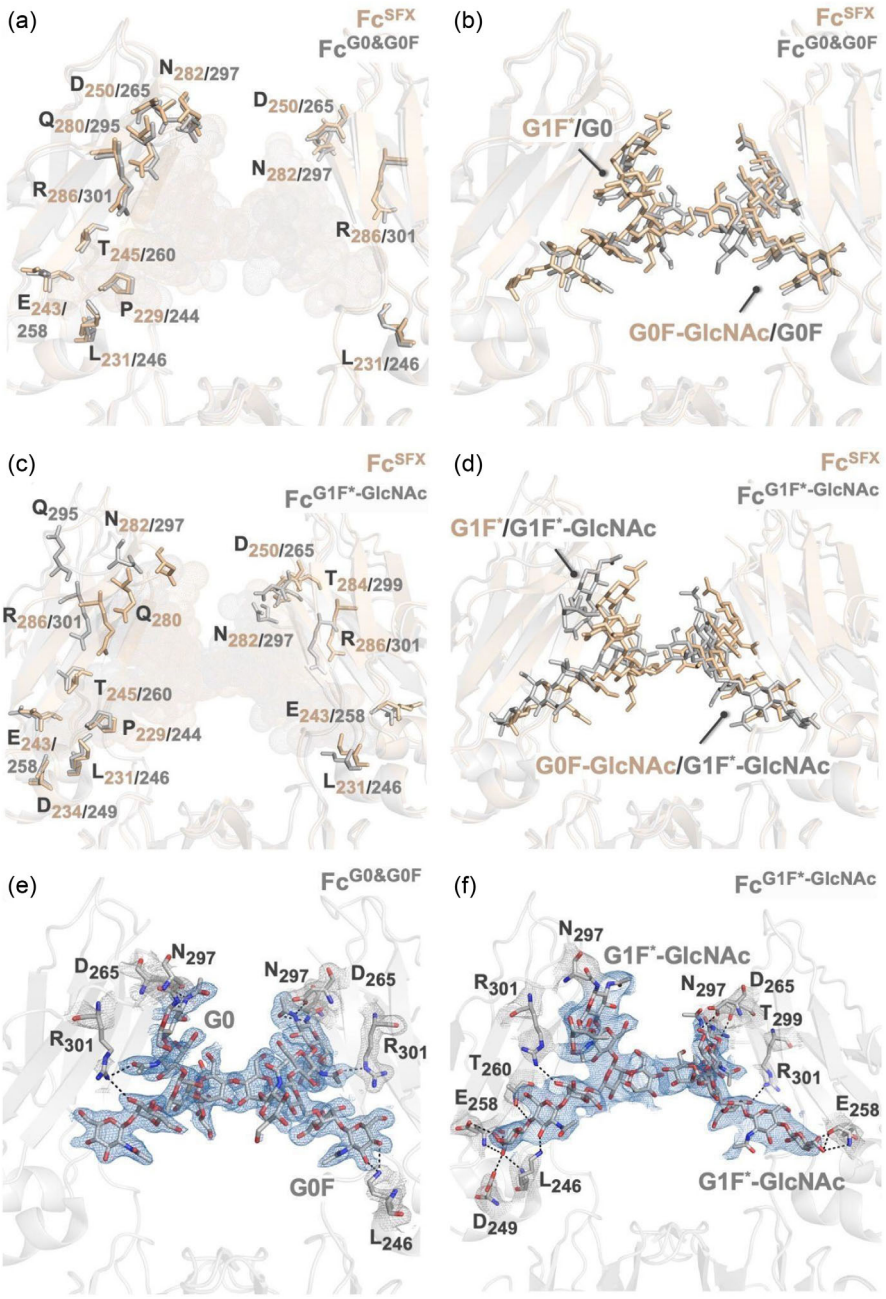


Figure 5. Comparison of the glycan-binding site of Fc^{SFX} with $Fc^{G0\&G0F}$ and $Fc^{G1F*-GlcNAc}$ structures (PDB IDs: 4W4N&1H3V, respectively). a–d) Fc^{SFX} structure is superposed with $Fc^{G0\&G0F}$ and $Fc^{G1F*-GlcNAc}$ structures to highlight the conformational changes in the glycan-binding site. e,f) The critical residues during the interaction with N-glycans are indicated for $FC^{G0\&G0F}$ and $FC^{G1F*-GlcNAc}$ structures. Polar contacts are shown with black dashed lines. The 2Fo-Fc electron densities are contoured at 1 σ level and colored in sky blue (N-glycans) and gray (protein residues). Fc^{SFX} structure is colored wheat while $Fc^{G0\&G0F}$ and $Fc^{G1F*-GlcNAc}$ structures are colored gray. PDB IDs and GlyTouCan IDs are indicated in Table S2, Supporting Information.

B_{Damage} that summarizes the extent of specific radiation damage. Accordingly, both cryogenic and ambient temperature structures have low radiation damage values ($B_{net} = 0.9–1.5$) based on the data collection setup.[44] These findings indicate the high *b*-factor values mostly correlated with the mobility of the structure.

$Fc^{Synchrotron}$ and $Fc^{XRD(Cryogenic)}$ structures are superposed with previously published cryogenic temperature structures (Figure S13 and S14, Supporting Information). Based on the comparison of $Fc^{Synchrotron}$ and $Fc^{G0\&G0F}$ structures, minor conformational changes with 0.604 Å RMSD were observed in the glycan-binding site residues, except for the L_{231} residue (Figure S15c, Supporting Information). Apart from $Fc^{G0\&G0F}$structure, major conformational changes up to 0.922 Å were observed in $Fc^{G1F\&G0F}$ and $Fc^{G1F*-GlcNAc}$ structures (Figure S10c and S16c, Supporting Information). For the $Fc^{XRD(Cryogenic)}$ structure, similarly minor conformational changes with 0.422 Å RMSD were observed

© 2025 The Author(s). Small Structures published by Wiley-VCH GmbH

26884062, 2025, 8, Downloaded from https://onlinelibrary.wiley.com/doi/10.1002/sstr.202400680 by Koc University, Wiley Online Library on [19/08/2025]. See the Terms and Conditions (https://onlinelibrary.wiley.com/terms-and-conditions) on Wiley Online Library for rules of use; OA articles are governed by the applicable Creative Commons License

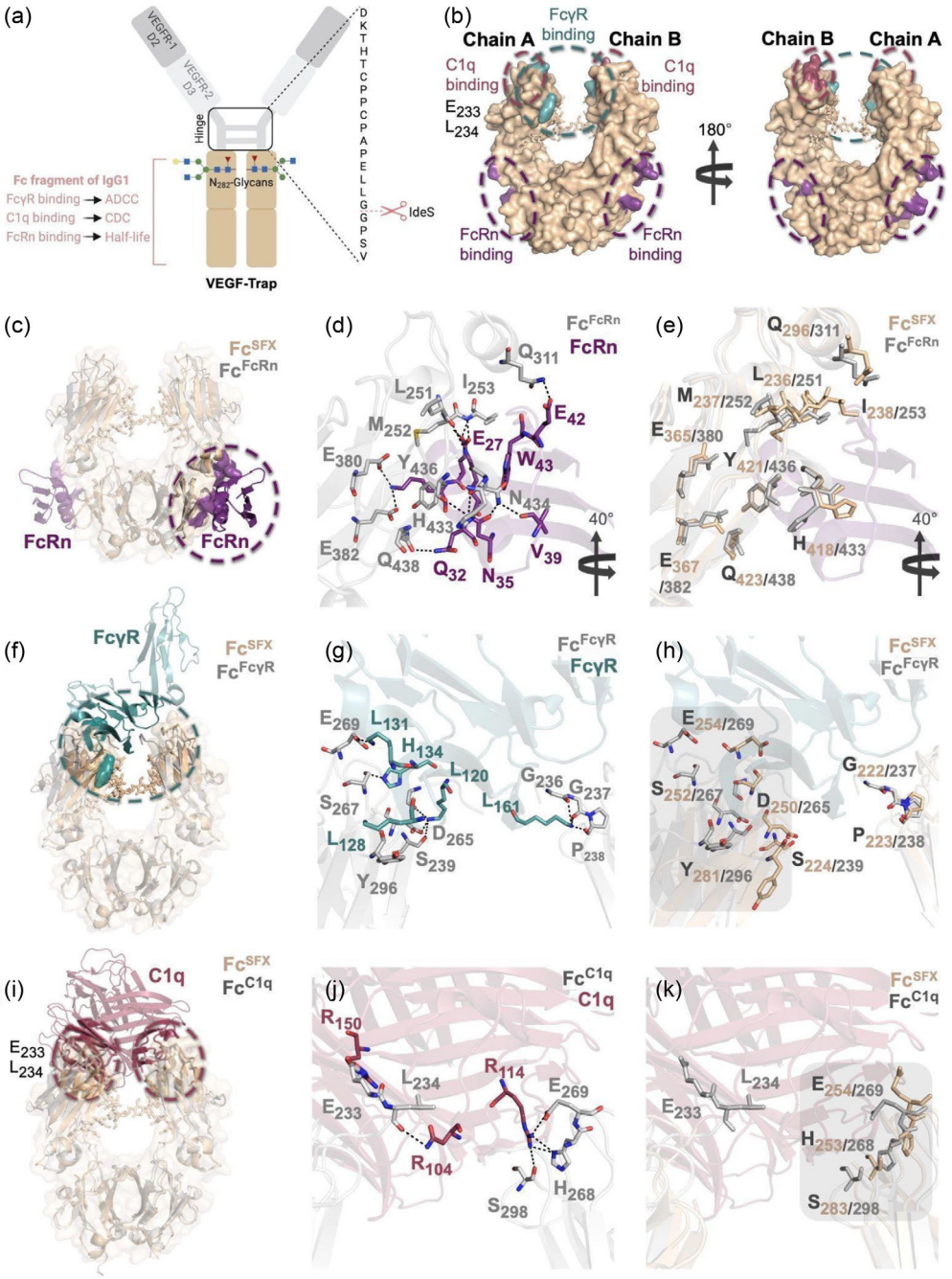


Figure 6. Conformational changes of the active site residues on Fc fragment in the presence of FcRn, FcγR, and C1q. a) The systematic representation of the VEGF-Trap is illustrated to indicate the cleavage site of IdeS protease for obtaining the Fc fragment. b) Fc fragment involves binding sites for FcRn, FcγR, and C1q. Fc^{SFX} structure is colored in wheat while FcRn, Fcγ, and C1q binding sites are colored in violet purple, light teal, and raspberry, respectively. c–e) Fc fragment of IgG1 subtype in complex with FcRn (Protein G-bound) (PDB ID: 1FCC) (Fc^{FcRn}) and Fc^{SFX} structures are superposed with RMSD value 0.873 Å. Fc^{FcRn} is colored in gray while FcRn binding region and Protein G are colored in violet purple. f–h) Fc fragment of IgG1 subtype in complex with FcγR (PDB ID: 7URU) ($Fc^{FcγR}$) and Fc^{SFX} structures are superposed with RMSD value 0.627 Å. $Fc^{FcγR}$ is colored gray while FcγR binding region is colored light teal. i–k) Fc fragment of IgG1 subtype in complex with C1q (PDB ID: 6FCZ) (Fc^{C1q}) and Fc^{SFX} structures are superposed with RMSD value 1.067 Å. Fc^{C1q} is colored gray while C1q binding region is colored raspberry. There is one available binding site for FcγR and two potential binding sites for C1q and FcRn per IgG1 molecule. C1q binding site in Chain A is not visible for Fc^{SFX} structure as E_{233} and L_{234} residues are located in the hinge region. Fc^{SFX} structure is colored in wheat. Polar contacts are shown with dashed black lines. As a result of superposition, the major shifts in the secondary structures are indicated with gray squares.

© 2025 The Author(s). Small Structures published by Wiley-VCH GmbH

26884062, 2025, 8, Downloaded from https://onlinelibrary.wiley.com/doi/10.1002/sstr.202400680 by Koc University, Wiley Online Library on [19/08/2025]. See the Terms and Conditions (https://onlinelibrary.wiley.com/terms-and-conditions) on Wiley Online Library for rules of use; OA articles are governed by the applicable Creative Commons License

compared to the $Fc^{G0\&G0F}$ structure while major conformational changes up to 0.866 Å were observed in $Fc^{G1F\&G0F}$ and $Fc^{G1F^*-GlcNAc}$ structures (Figure S10e, S15e, and S16e, Supporting Information). These findings indicate the different structural conformation based on N-glycan composition (Figure S10, S15, and S16, Supporting Information).

2.3. Superposition with Previously Published Structures Reveals the Conformational Changes upon Binding to FcRn, FcγR, or C1q Proteins

The Fc fragment of the IgG1 subtype is a common scaffold for designing recombinant proteins.[14] It has binding sites for neonatal Fc receptor (FcRn), FcγR, and complement protein C1q, which are essential for immune system function (**Figure 6**a).[24] Since N-glycosylation influences protein stability, understanding how proteins undergo conformational changes during these interactions plays a vital role. Here, we compared our N-glycan-bound structures with previously available complex structures and generated molecular morphs between the two conformations to observe the transition from the unbound to the bound state. The observed conformational changes at the interaction sites in the absence of FcRn, FcγR, and C1q proteins highlighted the structural dynamics of this transition.

Each IgG1 molecule has one binding site for FcγR and two putative binding sites for C1q and FcRn (Figure 6b). The superposition of our structures with FcRn-bound structure (PDB ID: 1FCC) (Fc^{FcRn}) revealed the major conformational changes on the key residues (L_{236}, M_{237}, I_{238}, Q_{296}, E_{367}, and H_{418}) during the binding of FcRn (Figure 6c–e, S17a,d, S18a,d, S19a,d, and Movie S1, S2, Supporting Information). A close look at the FcRn binding site for both ambient and cryogenic temperature structures indicated similarly significant conformational changes. Differently, Y_{421} maintains its position in the ambient temperature structures while it has slightly altered conformation in the cryogenic temperature structures. These findings indicate the loop in which Y_{421} is located and continues with beta-strand maintains its stability while the regions around the residues L_{236}-Q_{296} and H_{418} undergo backbone displacement during the transition to the FcRn-bound state. For the FcγR binding site, significant conformational changes were observed in the loop region of chain A near the glycan-binding site for both ambient and cryogenic temperature structures (Figure 6f–h, S17b,e, S18b,e, S19b,e and Movie S3, S4, Supporting Information). The S_{224}, D_{250}, S_{252}, E_{254}, and Y_{281} residues in the loop are shifted in the presence of FcγR binding (PDB ID: 7URU) ($Fc^{FcγR}$) while Chain B near to interaction site was detected as more stable. Although the C1q protein has two binding sites for

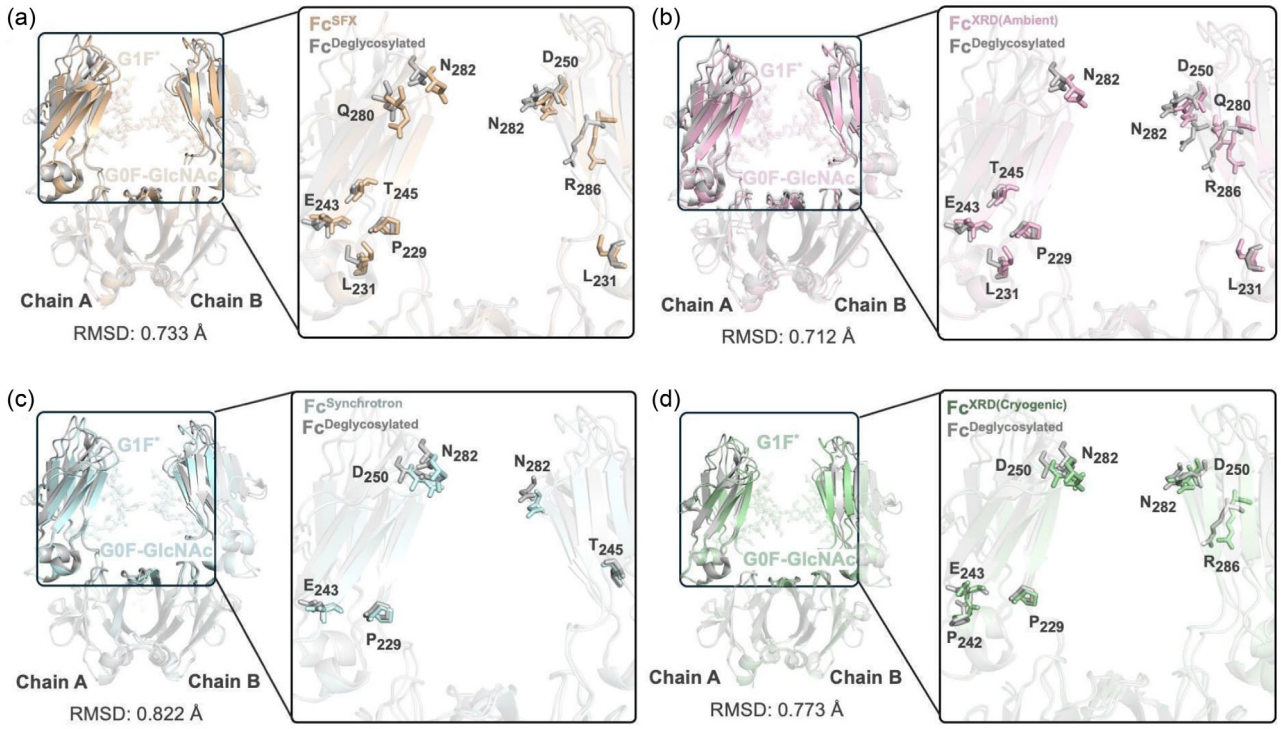


Figure 7. Conformational changes on the residues that interact with N-glycans (G1F* & G0F-GlcNAc). a) Fc^{SFX} structure is superposed with deglycosylated structure (PDB ID: 7HRO) ($Fc^{Deglycosalated}$) and glycan-binding site residues are indicated in stick representation. The Fc^{SFX} structure is colored in wheat while the $Fc^{Deglycosalated}$ structure is colored gray. b) $Fc^{XRD(Ambient)}$ structure is superposed with $Fc^{Deglycosalated}$ structure and glycan-binding site residues are indicated in stick representation. $Fc^{XRD(Ambient)}$ structure is colored light pink while the $Fc^{Deglycosalated}$ structure is colored gray. c) $Fc^{Synchrotron}$ structure is superposed with $Fc^{Deglycosalated}$ structure and glycan-binding site residues are indicated in stick representation. The $Fc^{Synchrotron}$ structure is colored in pale cyan while the $Fc^{Deglycosalated}$ structure is colored gray. d) $Fc^{XRD(Cryogenic)}$ structure is superposed with $Fc^{Deglycosalated}$ structure and glycan-binding site residues are indicated in stick representation. The $Fc^{XRD(Cryogenic)}$ structure is colored pale green while the $Fc^{Deglycosalated}$ structure is colored gray.

© 2025 The Author(s). Small Structures published by Wiley-VCH GmbH

26884062, 2025, 8, Downloaded from https://onlinelibrary.wiley.com/doi/10.1002/sstr.202400680 by Koc University, Wiley Online Library on [19/08/2025]. See the Terms and Conditions (https://onlinelibrary.wiley.com/terms-and-conditions) on Wiley Online Library for rules of use; OA articles are governed by the applicable Creative Commons License

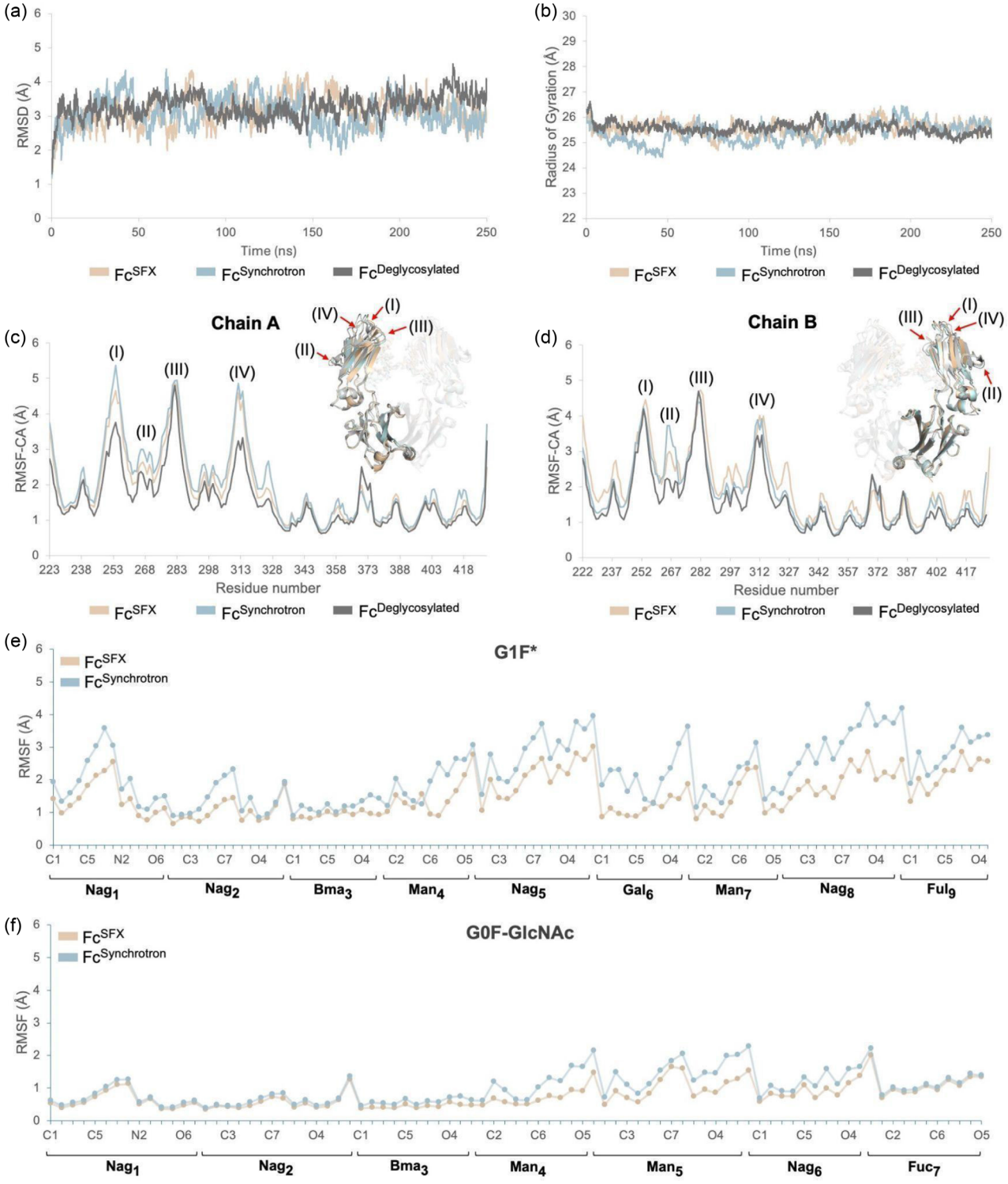


Figure 8. Structural dynamic differences in the presence of N-glycans based on molecular dynamics simulations. The result of three production runs (total of 750 ns) is averaged and the deglycosylated Fc fragment from IgG1 subtype (PDB ID: 7RHO) ($Fc^{Deglycosylated}$) is used as a reference structure for the analysis. a,b) RMSD (Å) and radius of gyration (Å) are calculated for each structure to reveal the protein compactness through the simulation period (250 ns). c,d) RMSF (Å) is calculated for each chain based on alpha carbons. High-fluctuated regions are indicated with red arrows. e,f) RMSF (Å) is calculated for N-glycans which are bound to chain A (G1F*) and chain B (G0F-GlcNAc). The calculation is performed for each atom that builds the residues of N-glycan.

© 2025 The Author(s). Small Structures published by Wiley-VCH GmbH

26884062, 2025, 8, Downloaded from https://onlinelibrary.wiley.com/doi/10.1002/sstr.202400680 by Koc University, Wiley Online Library on [19/08/2025]. See the Terms and Conditions (https://onlinelibrary.wiley.com/terms-and-conditions) on Wiley Online Library for rules of use; OA articles are governed by the applicable Creative Commons License

chains A and B, the chain A binding site is not visible as it is located in the hinge region. Cryo-EM structure of C1q-Fc complex structure (PDB ID: 6FCZ) (Fc^{C1q}) was superposed with our structures (Figure 6i–k, S17c,f, S18c,f, S19c,f and Movie S5, S6, Supporting Information). The major conformational changes on the E_{254}, H_{253}, and S_{283} residues were observed for both ambient and cryogenic temperature structures when it is in complex with C1q. This finding indicates that the binding of C1q leads to the backbone displacement in Chain B.

2.4. MD Simulations Highlight the Details of Glycan-Binding Pocket Dynamics and Interdomain Motions

The comparison of G1F* and G0F-GlcNAc-bound structures with the $Fc^{Deglycosylated}$ structure indicated significant conformational changes in the glycan-binding site (**Figure 7**). Especially, N_{282} which plays a key role during the N-glycosylation process was detected as a major conformational change, indicating the movement of the loop region during the glycan binding (Movie S7–S10, Supporting Information). To highlight the binding mechanism of N-glycans, MD simulations were performed using Fc^{SFX}, $Fc^{Synchrotron}$, and $Fc^{Deglycosylated}$ structures. As we observed altered N-glycan conformation at cryogenic temperature, computational observation of $Fc^{Synchrotron}$ structure offers a new insight due to the effect that the initial structure lacks some glycan-amino acid linkages. RMSD (Å) calculation based on the backbone atoms of each protein indicated the stable maintenance of the conformations (**Figure 8**a and S20a–c, Supporting Information). To detect the structural changes through 250 ns, a radius of gyration (Å) calculation based on the center of mass of each atom in the molecule was performed, providing initial information about the molecule's overall shape and compactness. While there is no major difference between Fc^{SFX} and $Fc^{Deglycosylated}$ structures, a small jump was detected in the fiftieth nanosecond for the $Fc^{Synchrotron}$ structure (Figure 8b and S20d–f, Supporting Information). Following the jump, this change in compactness converges back to the initial state, indicating secondary structure stabilization. As the next step, highly flexible regions were revealed by root-mean-square-fluctuation (RMSF)-CA (Å) calculation. It is observed that three loop regions (I, III, IV) near the glycan-binding site are more flexible for both chains compared to the rest of the molecule (Figure 8c,d). Within these regions, I (residue range: 244–262) and IV (residue range: 306–321) regions in chain A were detected as ≈1.5-fold more flexible compared to the $Fc^{Deglycosylated}$ structure, indicating the effect of long-chain N-glycan (G1F*). For chain B where the short-chain glycan (G0F-GlcNAc) is bound, the loop region II (residue range: 264–272) was detected as more flexible compared to both the $Fc^{Deglycosylated}$ structure and chain A of Fc^{SFX}, $Fc^{Synchrotron}$ structures. These findings indicate that the binding of N-glycans causes additional flexibility on the protein, supporting the previous results from X-Ray crystallography data (Figure 3).

Atom versus RMSF (Å) values were calculated for N-glycans to detect fluctuations of atoms during the simulation time frame (Figure 8e,f). It is observed that G0F-GlcNAc which bound the chain B is more stable compared to G1F*, explaining the weak electron density for G1F* in the chain A. To provide a better understanding of conformational changes in the presence of N-glycans, the frames of production run 3 (R3) were analyzed in detail (Movie S11–S13, Supporting Information). It is observed that the addition of G1F* causes a significant displacement in chain A (especially the C_H2 domain) while chain B maintains its stability (Figure S21 and S22, Supporting Information). These dynamics in the presence of N-glycans may induce the binding of other partners to the Fc region in the immune system.[45] Based on atom versus RMSF(Å) values, glycan binding to the critical residues does not interfere with the general trend that surface exposed residues becoming more flexible than buried ones compared with the $Fc^{Deglycosylated}$ structure (Figure S23a–h, Supporting Information). However, RMSF-CA (Å) and RMSF-Side Chain (Å) calculations revealed differences, supporting the chain movement in the C_H2 domain. It is observed that D_{250} is more flexible while N_{282} is more stable in the presence of N-glycans (Figure S23i–l and Table S3, Supporting Information). Additionally, distances were calculated between the critical residues and N-glycans to determine the stability of the polar contacts (Figure S24, Supporting Information). Comparison of distance measurements for the residues P_{229}, L_{231}, E_{243}, and T_{245} in chain A indicated that the flexible G1F* glycan returns back to a close position with these residues for the $Fc^{Synchrotron}$ structure while it tends to move away for the Fc^{SFX} structure. Overall, these counter motions once again show us interaction patterns of flexible G1F* (Figure S25, Supporting Information). For chain B, as G0F-GlcNAc is less flexible in the glycan-binding pocket, the distances were detected as stable throughout the simulation period (Figure S26, Supporting Information). These findings indicated the unstable state of the long-chain ligand.

3. Conclusions

The data presented herein offers a comprehensive analysis of the binding mechanism of N-glycans and its effects on protein structure. Insights into how N-glycans induce conformational changes may enable the engineering of drugs with optimized potency, stability, efficacy, and pharmacokinetics. For this purpose, the near-physiological structure is essential as it closely mimics the near-natural conformation. The experimental and computational observation of the structural dynamics revealed that the binding of long and short-chain N-glycans differently affects the stability of the Fc fragment of the IgG1 subtype from biosimilar VEGF-Trap. Specifically, it was found that long-chain N-glycan (G1F*) in Chain A destabilizes the Fc fragment, which may weaken the protein's overall structural integrity. In contrast, short-chain N-glycan (G0F-GlcNAc) in Chain B appears to stabilize the Fc fragment more effectively. The optimization of glycan structures on the Fc fragment can improve binding specificity and strength, enhancing the therapeutic's potency while minimizing the risk of immune-related side effects.

4. Experimental Section

Protein Sample Preparation: Full-length biosimilar VEGF-Trap protein (40 mg mL^{-1}) which is produced by our DEVA Holding AS team in Türkiye was incubated with 10 µL IdeS protease (PROMEGA, USA) for 3 h at 37 °C to cleave the Fc region below hinge region, generating the

© 2025 The Author(s). Small Structures published by Wiley-VCH GmbH

26884062, 2025, 8, Downloaded from https://onlinelibrary.wiley.com/doi/10.1002/sstr.202400680 by Koc University, Wiley Online Library on [19/08/2025]. See the Terms and Conditions (https://onlinelibrary.wiley.com/terms-and-conditions) on Wiley Online Library for rules of use; OA articles are governed by the applicable Creative Commons License

binding domains of VEGFR-1 and VEGFR-2 and Fc fragment. Further, the size exclusion chromatography method was applied to purify the ≈50 kDa Fc fragment. Superdex 200 (S200) column was used with the buffer containing 150 mM NaCl and 20 mM Tris–HCI (pH 6.2). Elutions were collected for each peak and the Fc fragment peak was inspected using SDS-PAGE. Finally, the pure protein was pooled and concentrated by Amicon ultrafiltration 30 kDa cutoff spin filters from Millipore to a final concentration of 10 mg mL^{-1} and stored at −80 °C until crystallization trials.

Crystallization: Sitting-drop vapor diffusion micro-batch under the oil technique was used for initial crystallization screening as explained by Ertem et al.[46] Purified Fc protein at 10 mg mL^{-1} mixed with ≈ 3500 commercially available sparse matrix crystallization screening conditions (1:1 v v^{-1}) in a 72-well Terasaki plate (Greiner-Bio, Germany). Then, each well was covered with 16.6 µL paraffin oil (Tekkim Kimya, Turkiye) and incubated at room temperature. The best crystals were obtained at Index crystallization screen 1 condition #43, containing 0.1 M Bis–Tris (pH 6.5), 25% w/v polyethylene glycol (PEG) 3350, from Hampton Research, USA (Figure S2a, Supporting Information). Replica plates were done by using the same crystallization screen condition. After multiple optimizations of the seeding protocol by using crystals obtained by microbatch under oil, we scaled up the batch crystallization volume to a total of 1.5 mL. During the scale-up process, the formation of microcrystals was observed by a compound light microscope (Figure S2b, Supporting Information).

Ambient and Cryogenic-Temperature Data Collection and Data Processing at Turkish DeLight: Initial ambient-temperature data was collected by using Rigaku's XtaLAB Synergy Flow XRD system controlled by CrysAlisPro software (Rigaku Oxford Diffraction, 2022) as described by Gul et al.[29] The airflow temperature of Oxford Cryosystems's Cryostream 800 Plus was adjusted to 300 K (26.85 °C) and the 72-well Terasaki plate was placed on the modified adapter of the XtalCheck-S plate reader. After selecting well-diffracting crystals, diffraction data were collected from multiple crystals by using automatic data collection mode. During the data collection, the detector distance was set at 100.00 mm and exposure time was 5.00 s per image. The diffraction data was collected with different scan widths (0.10°, 0.20°, and 0.50°) and X-Ray intensities (2, 4, and 10%). A total of 14 898 frames were collected in 20 h. The collected data was processed using the automatic data reduction process and merged using the proffit merge process of CrysAlisPro software (Rigaku Oxford Diffraction, 2022). For cryogenic temperature data collection from a single crystal, Oxford Cryosystems's Cryostream 800 Plus was adjusted to 100 K and data was collected as described by Atalay et al.[47] A total of 720 frames were collected in 32 min.

Cryogenic-Temperature Data Collection and Processing at Spring-8: Diffraction data from multiple crystals was collected at the BL32XU beamline at SPring-8 using the automated data-collection system ZOO described by Hirata et al.[32] Before the data collection, crystals were frozen in liquid nitrogen and pucks were replaced into the dewar which is filled with liquid nitrogen in the hutch. All data sets were acquired using a continuous helical scheme with 360° of oscillation and the following experimental parameters: oscillation width, 0.1°; exposure time, 0.02 s; beam size, 10 µm (horizontal) × 15 µm (vertical); wavelength, 1 Å; average dose per crystal volume, 10 M Gy; detector, EIGER X 9M (Dectris); temperature, 100 K. The data obtained were automatically processed by XDS[48] in KAMO.[31]

SFX Data Collection and Processing at SACLA: Diffraction data from microcrystals was collected at the Experimental Hutch 3 of SACLA Beamline 2 using 10 keV X-rays with a pulse duration of <10 fs and a repetition rate of 30 Hz.[49,50] To obtain 10^8 crystal density for SFX experiments, 500 µL microcrystal slurry was centrifuged at 3000 rpm for 5 min, and 490 µL supernatant was discarded for each injection. The remaining 10 µL crystal slurry with 10^8 crystal density was mixed with grease (No. 42150, Synco Chemical Co.) on a plastic plate according to a previously reported procedure (Figure S2c, Supporting Information).[51] The sample was directly transferred into a 200 µL sample cartridge carefully by using a spatula without leaving any bubbles inside the sample-grease mix. Then, the cartridge was loaded into the HVC injector with a nozzle of 75 µm ID. The HVC injector was installed in a He-gas-filled diffraction chamber of the DAPHNIS instrument.[37] Diffraction patterns were recorded using the MPCCD detector at a sample-to-detector distance of 50 mm.[52] HPLC flow rate was set as 0.0127 µL min^{-1} and the sample slurry (mixed with grease) was injected at a flow rate of 0.79 µL min^{-1}. Diffraction images were filtered to extract "hit" images through the CHEETAH[53] pipeline at SACLA and indexed by using CrystFEL.[54–56] During the beamtime, three injections were done and a total of 24 873 out of 66 849 hits were indexed. Final data processing and merging were performed using CrystFEL.

Structure Determination and Refinement: Four structures of the Fc fragment of IgG1 subtype from VEGF-Trap were determined in space group $P2_12_12_1$ by using the automated molecular replacement program PHASER[57] implemented in PHENIX[58] suite. The coordinates of previously published cryogenic-temperature structure (PDB ID: 4W4N) ($Fc^{G0\&G0F}$) were used for initial rigid body refinement. After simulated-annealing refinement, individual coordinates and TLS parameters were refined. N-glycans were replaced into the structure and altered side chains and water molecules were checked in COOT.[59] The positions with strong difference density were retained and water molecules located outside of significant electron density were manually removed. Data collection and structure refinement statistics are summarized in Table S1, Supporting Information. For the structural alignments and figure generation, PyMOL[60] was used and secondary structure alignment was performed by using JALVIEW.[61] Quantification of radiation damage for each structure was performed by using RABDAM software,[43] and all kernel density plots were drawn by using MATLAB.[62]

MD Simulations and Data Analysis: All MD simulations were performed by using the Nanoscale Molecular Dynamics (NAMD 3.0) program[63] with the CHARMM36m[64] force field. Preprocessing of the structures (protein and N-glycans) including the addition of solvation box and ions was completed through Input Generator/Solution Builder of CHARMM-GUI.[65] The TIP3P model was used for water molecules within the system during the simulation. The system size (cubic) was determined to have at least 10 Å from protein in all axes and 150 mM NaCl was added for neutralization of charge. Protonation states of the histidines were determined using PDB2PQR software.[66] Disulphide bridges were formed based on the structural information provided within the PDB files. In the deglycosylated cryogenic temperature structure (PDB ID: 7RHO) ($Fc^{Deglycosylated}$) only, protein chains were completed for 2–3 missing amino acid residues in N and C terminal ends, respectively. Systems were fully energy minimized 10 000 steps with the conjugate gradient method, which was followed by equilibration with 125 000 steps of canonical (NVT) ensemble.[67] During equilibration, protein positional restraints and carbohydrate dihedral restraints were employed as provided by CHARMM-GUI output. For production simulations, an isothermal-isobaric (NPT) ensemble was employed with periodic boundary conditions and Coulomb interactions were calculated using the particle-mesh Ewald algorithm.[68] 10 Å of switching distance and 12 Å of cutoff distance limits were used to calculate nonbonded electrostatic interactions and Van der Waals interactions. The pressure was held at 1 atm using the Nose–Hoover Langevin method and the temperature was kept at 310 K with Langevin dynamics.[69] Lengths of the hydrogen-containing bonds were constrained using the SHAKE algorithm.[70] A 2 fs time step was used in all simulations. The production runs were set as 250 ns in triplicates. In total, 750 ns MD simulation was performed for each structure and the total run time was 2.25 µs.

VMD software[71] was used for the analysis of trajectories and the visualization of structures. RMSD calculations were performed to determine conformational stability through 250 ns MD simulations. Before each calculation, the structure was aligned to the initial frame and RMSD was calculated based on the backbone atoms for each production run by using the RMSD trajectory tool module of VMD. The radius of gyration was calculated based on the center of mass to characterize the spatial conformation and measure the compactness. The RMSF and distance calculations were performed to reveal the details of structural dynamics in the glycan-binding site. All the calculations in the study were computed with tcl scripts. As there are three production runs for each structure, the results were averaged and considered for the interpretation of the data. All simulation movies were generated by using the movie maker module of VMD.

© 2025 The Author(s). Small Structures published by Wiley-VCH GmbH

26884062, 2025, 8, Downloaded from https://onlinelibrary.wiley.com/doi/10.1002/sstr.202400680 by Koc University, Wiley Online Library on [19/08/2025]. See the Terms and Conditions (https://onlinelibrary.wiley.com/terms-and-conditions) on Wiley Online Library for rules of use; OA articles are governed by the applicable Creative Commons License

Supporting Information

Supporting Information is available from the Wiley Online Library or from the author.

Acknowledgements

This publication has been produced benefiting from the 2244 Industrial Ph.D. Fellowship Program Funding Program of the Scientific and Technological Research Council of Turkey (TÜBİTAK) (Project Numbers: 119C132). However, the entire responsibility of the publication belongs to the owner of the publication. The financial support received from TÜBİTAK does not mean that the content of the publication is approved in a scientific sense by TÜBİTAK. Portions of this research were carried out at the SPring-8 Angstrom Compact free electron LAser, Japan (SACLA), and supported by the SACLA Research Support Program for Graduate Students (Proposal numbers: 2023B8058 and 2023B2761). The authors gratefully acknowledge the use of the services and Turkish Light Source (Turkish DeLight) X-Ray facility at the University of Health Sciences, Experimental Medicine Application & Research Center (DETUAM), Validebag Research Park. The authors thank Jerome Johnson for his help during cryogenic temperature data collection at Turkish DeLight. The numerical calculations reported in this work were fully performed at TUBITAK ULAKBIM, High Performance and Grid Computing Center (TRUBA resources).

Conflict of Interest

The authors declare no conflict of interest.

Author Contributions

The project was initiated and coordinated by Hasan DeMirci and Irfan Cinkaya. Fc fragment of VEGF-Trap is purified by Ebru Destan, Engin Turkut, Alper Aldeniz, Baris Yilmaz, and Irfan Cinkaya. Diffracting crystals were obtained and optimized by Ebru Destan. Crystallography applications at SPring-8/SACLA were supported by Ebru Destan, Jungmin Kang, Takehiko Tosha, and Makina Yabashi, and in beamtime, samples were prepared by Ebru Destan. SFX data at SACLA was collected by Ebru Destan and Jungmin Kang. Synchrotron data at SPring-8 was collected by Ebru Destan, Jungmin Kang, and Takehiko Tosha with the help of Yoshiaki Kawano. Crystallography applications at Turkish DeLight were supported by Ebru Destan and Hasan DeMirci, and in beamtime, samples were prepared by Ebru Destan and the data were collected by Ebru Destan and Hasan DeMirci. The data processing was performed for SFX and XRD structures by Ebru Destan and for synchrotron structure by Hiroaki Matsuura. Structures were refined by Ebru Destan, and data were interpreted by Ebru Destan with the help of Hasan DeMirci and Irfan Cinkaya. Molecular dynamics simulations were performed by Ahmet Can Timucin, and data were analyzed and interpreted by Ebru Destan and Ahmet Can Timucin. All of the authors read and acknowledged the manuscript.

Data Availability Statement

Coordinates and structure factors have been deposited in the RCSB Protein Data Bank under accession codes 8ZCK and 8ZCL, which correspond to the ambient temperature structures (Fc^{SFX} and $Fc^{XRD(Ambient)}$, respectively); and 8ZCM and 9IIE, which correspond to the cryogenic structures ($Fc^{Synchrotron}$ and $Fc^{XRD(Cryogenic)}$, respectively).

Keywords

immunoglobulin, N-glycosylation, protein dynamics, structural biology

Received: December 22, 2024
Revised: February 4, 2025
Published online: April 22, 2025

[1] H. Zheng, K. B. Handing, M. D. Zimmerman, I. G. Shabalin, S. C. Almo, W. Minor, *Expert Opin. Drug Discov.* **2015**, *10*, 975.
[2] H. N. Chapman, P. Fromme, A. Barty, T. A. White, R. A. Kirian, A. Aquila, M. S. Hunter, J. Schulz, D. P. Deponte, U. Weierstall, R. B. Doak, F. R. N. C. Maia, A. V. Martin, I. Schlichting, L. Lomb, N. Coppola, R. L. Shoeman, S. W. Epp, R. Hartmann, D. Rolles, A. Rudenko, L. Foucar, N. Kimmel, G. Weidenspointner, P. Holl, M. Liang, M. Barthelmess, C. Caleman, S. Boutet, M. J. Bogan, et al., *Nature* **2011**, *470*, 73.
[3] L. C. Johansson, B. Stauch, A. Ishchenko, V. Cherezov, *Trends Biochem. Sci.* **2017**, *42*, 749.
[4] E. Mizohata, T. Nakane, Y. Fukuda, E. Nango, S. Iwata, *Biophys. Rev.* **2018**, *10*, 209.
[5] I. Yapici, E. H. Dao, S. Yokoi, E. Destan, E. Ayan, A. Shafei, F. B. Ertem, C. Kulakman, M. Yilmaz, B. Tosun, H. Ciftci, A. Kepceoglu, J. Johnson, O. Guven, A. Ergul, B. Hayes, Y. Rao, C. Kupitz, F. P. Poitevin, H. DeMirci, *4D Crystallography Captures Transient IF1-Ribosome Dynamics in Translation Initiation*, bioRxiv **2023**, 10.27.564398.
[6] M. E. O'Sullivan, F. Poitevin, R. G. Sierra, C. Gati, E. H. Dao, Y. Rao, F. Aksit, H. Ciftci, N. Corsepius, R. Greenhouse, B. Hayes, M. S. Hunter, M. Liang, A. Mcgurk, P. Mbgam, T. Obrinsky, F. Pardo-Avila, M. H. M. Seaberg, A. G. Cheng, A. J. Ricci, H. Demirci, *Nucleic Acids Res.* **2018**, *46*, 9793.
[7] S. Durdagi, D. Çağdaş , D. Berna, Y. Merve, A. Timucin, B. Cengizhan, E. Ismail, B. E. Fatma, C. Seyma, Y. Gunseli, D. O. Muge, G. Guven, A. Busecan, D. Ebru, S. Kader, O. B. Sabri, O. Lalehan, S. Alaleh, T. Ilayda, A. Esra, Y. Busra, B. P. Ayse, G. Oktay, D. Y. Ali, C. Ozgur, O. Serena, O. Alpsu, E. Ece, A. Fulya, T. Gokhan, *Structure* **2021**, *29*, 1382.
[8] C. A. Black, *Immunol. Cell Biol.* **1997**, *75*, 65.
[9] J. Tellier, S. L. Nutt, *Eur. J. Immunol.* **2019**, *49*, 30.
[10] Lenette L. Lu, T. J. Suscovich, S. M. Fortune, G. Alter, *Nat. Rev. Immunol.* **2018**, *18*, 46.
[11] X. Chi, Y. Li, X. Qiu, *Immunology* **2020**, *160*, 233.
[12] D. Jung, F. W. Alt, *Cell* **2004**, *116*, 299.
[13] C. H. Bassing, W. Swat, F. W. Alt, *Cell* **2002**, *109*, S45.
[14] E. Lobner, M. W. Traxlmayr, C. Obinger, C. Hasenhindl, *Immunol. Rev.* **2016**, *270*, 113.
[15] Y. Tang, P. Cain, V. Anguiano, J. J. Shih, Q. Chai, Y. Feng, *MAbs* **2021**, *13*, 1993768.
[16] K. Spilsbury, K. L. Garrett, W.-Y. Shen, I. J. Constable, P. E. Rakoczy, *Am. J. Pathol.* **2000**, *157*, 135.
[17] C. N. Nagineni, V. K. Kommineni, A. William, B. Detrick, J. J. Hooks, *J. Cell. Physiol.* **2012**, *227*, 116.
[18] K. L. Meadows, H. I. Hurwitz, *Cold Spring Harb. Perspect. Med.* **2012**, *2*, a006577.
[19] J. S. Rudge, G. Thurston, S. Davis, N. Papadopoulos, N. Gale, S. J. Wiegand, G. D. Yancopoulos, *Cold Spring Harb. Symp. Quant. Biol.* **2005**, *70*, 411.
[20] M. Ohr, P. K. Kaiser, *Ther. Adv. Chronic Dis.* **2012**, *3*, 153.
[21] P. Gogesch, S. Dudek, G. Van Zandbergen, Z. Waibler, M. Anzaghe, *Int. J. Mol. Sci.* **2021**, *22*, 8947.
[22] J. Yu, Y. Song, W. Tian, *J. Hematol. Oncol.* **2020**, *13*, 45.
[23] S. Bournazos, D. J. Dilillo, J. V. Ravetch, *J. Exp. Med.* **2015**, *212*, 1361.

© 2025 The Author(s). Small Structures published by Wiley-VCH GmbH

26884062, 2025, 8, Downloaded from https://onlinelibrary.wiley.com/doi/10.1002/sstr.202400680 by Koc University, Wiley Online Library on [19/08/2025]. See the Terms and Conditions (https://onlinelibrary.wiley.com/terms-and-conditions) on Wiley Online Library for rules of use; OA articles are governed by the applicable Creative Commons License

[24] K. O. Saunders, *Front. Immunol.* **2019**, *10*, 1296.
[25] D. Kao, H. Danzer, M. Collin, A. Groß, J. Eichler, J. Stambuk, G. Lauc, A. Lux, F. Nimmerjahn, *Cell Rep.* **2015**; *13*, 2376.
[26] T. T. Wang, *Curr. Top. Microbiol. Immunol.* **2019**, *423*, 63.
[27] J. Hodoniczky, Y. Z. Zheng, D. C. James, *Biotechnol. Prog.* **2005**, *21*, 1644.
[28] T. T. Wang, J. V. Ravetch, *J. Clin. Invest.* **2019**, *129*, 3492.
[29] M. Gul, E. Ayan, E. Destan, J. A. Johnson, A. Shafiei, A. Kepceoğlu, M. Yilmaz, F. B. Ertem, M. Yapici, B. Tosun, N. Baldir, N. Tokay, Z. Nergiz, G. Karakadioğlu, S. S. Paydos, C. Kulakman, C. K. Ferah, Ö. Güven, N. Atalay, E. K. Akcan, H. Cetinok, N. E. Arslan, K. Şabanoğlu, B. Aşçi, S. Tavli, H. Gümüsboğa, S. Altuntaş, M. Otsuka, M. Fujita, S. Tekin, et al., *Sci. Rep.* **2023**, *13*, 8123.
[30] K. Nass, *Acta Crystallogr. Sect. D Struct. Biol.* **2019**, *75*, 211.
[31] K. Yamashita, K. Hirata, M. Yamamoto, *Acta Crystallogr. D, Struct. Biol.* **2018**, *74*, 441.
[32] K. Hirata, K. Yamashita, G. Ueno, Y. Kawano, K. Hasegawa, T. Kumasaka, M. Yamamoto, *Acta Crystallogr. D Struct. Biol.* **2019**, *75*, 138.
[33] D. A. Keedy, H. Van Den Bedem, D. A. Sivak, G. A. Petsko, D. Ringe, M. A. Wilson, J. S. Fraser, *Structure* **2014**, *22*, 899.
[34] E. De La Mora, N. Coquelle, C. S. Bury, M. Rosenthal, J. M. Holton, I. Carmichael, E. F. Garman, M. Burghammer, J.-P. Colletier, M. Weik, *Proc. Natl. Acad. Sci.* **2020**, *117*, 4142.
[35] J. Coe, P. Fromme, *Protein Pept. Lett.* **2016**, *23*, 255.
[36] Y. Shimazu, K. Tono, T. Tanaka, Y. Yamanaka, T. Nakane, C. Mori, K. Terakado Kimura, T. Fujiwara, M. Sugahara, R. Tanaka, R. B. Doak, T. Shimamura, S. Iwata, E. Nango, M. Yabashi, *J. Appl. Crystallogr.* **2019**, *52*, 1280.
[37] K. Tono, E. Nango, M. Sugahara, C. Song, J. Park, T. Tanaka, R. Tanaka, Y. Joti, T. Kameshima, S. Ono, T. Hatsui, E. Mizohata, M. Suzuki, T. Shimamura, Y. Tanaka, S. Iwata, M. Yabashi, *J. Synchrotron Radiat.* **2015**, *22*, 532.
[38] H. S. Lee, W. Im, *Sci. Rep.* **2017**, *7*, 12659.
[39] A. S. More, R. T. Toth, S. Z. Okbazghi, C. R. Middaugh, S. B. Joshi, T. J. Tolbert, D. B. Volkin, D. D. Weis, *J. Pharm. Sci.* **2018**, *107*, 2315.
[40] V. A. Spiteri, J. Doutch, R. P. Rambo, J. Gor, P. A. Dalby, S. J. Perkins, *Biophys. J.* **2021**, *120*, 1814.
[41] M. Nagae, Y. Yamaguchi, *Int. J. Mol. Sci.* **2012**, *13*, 8398.
[42] E. F. Garman, *Biophys. Rev.* **2019**, *11*, 539.
[43] K. L. Shelley, T. P. E. Dixon, J. C. Brooks-Bartlett, E. F. Garman, *J. Appl. Crystallogr.* **2018**, *51*, 552.
[44] K. L. Shelley, E. F. Garman, *Nat. Commun.* **2022**, *13*, 1314.
[45] G. P. Subedi, A. W. Barb, *Structure* **2015**, *23*, 1573.
[46] F. B. Ertem, O. Guven, C. Buyukdag, O. Gocenler, E. Ayan, B. Yuksel, M. Gul, G. Usta, B. Cakılkaya, J. A. Johnson, E. H. Dao, Z. Su, F. Poitevin, C. H. Yoon, C. Kupitz, B. Hayes, M. Liang, M. S. Hunter, A. Batyuk, R. G. Sierra, G. Ketawala, S. Botha, Ç. Dağ, H. Demirci, *STAR Protoc.* **2022**, *3*, 101158.
[47] N. Atalay, E. Akcan, M. Gül, E. Ayan, E. Destan, F. Kuzucu, N. Tokay, B. Çakilkaya, Z. E. Nergiz, G. Usta, A. Kepceoğlu, İ. Yapici, B. Tosun, N. Baldir, G. Yildirim, J. Johnson, Ö. Güven, A. Shafiei, N. Arslan, M. Yilmaz, C. Kulakman, S. Paydos, S. Çinal, K. Şabanoğlu, A. Pazarçeviren, A. Yilmaz, B. Canbay, B. Aşçi, E. Kartal, S. Tavli, et al., *Turkish J. Biol.* **2023**, *47*, 1.
[48] W. Kabsch, *Acta Crystallogr. Sect. D Biol. Crystallogr.* **2010**, *66*, 125.
[49] T. Ishikawa, H. Aoyagi, T. Asaka, Y. Asano, N. Azumi, T. Bizen, H. Ego, K. Fukami, T. Fukui, Y. Furukawa, S. Goto, H. Hanaki, T. Hara, T. Hasegawa, T. Hatsui, A. Higashiya, T. Hirono, N. Hosoda, M. Ishii, T. Inagaki, Y. Inubushi, T. Itoga, Y. Joti, M. Kago, T. Kameshima, H. Kimura, Y. Kirihara, A. Kiyomichi, T. Kobayashi, C. Kondo, et al., *Nat. Photonics.* **2012**, *6*, 540.
[50] K. Tono, T. Togashi, Y. Inubushi, T. Sato, T. Katayama, K. Ogawa, H. Ohashi, H. Kimura, S. Takahashi, K. Takeshita, H. Tomizawa, S. Goto, T. Ishikawa, M. Yabashi, *New J. Phys.* **2013**, *15*, 083035.
[51] M. Sugahara, E. Mizohata, E. Nango, M. Suzuki, T. Tanaka, T. Masuda, R. Tanaka, T. Shimamura, Y. Tanaka, C. Suno, K. Ihara, D. Pan, K. Kakinouchi, S. Sugiyama, M. Murata, T. Inoue, K. Tono, C. Song, J. Park, T. Kameshima, T. Hatsui, Y. Joti, M. Yabashi, S. Iwata, *Nat. Methods.* **2015**, *12*, 61.
[52] T. Kameshima, S. Ono, T. Kudo, K. Ozaki, Y. Kirihara, K. Kobayashi, Y. Inubushi, M. Yabashi, T. Horigome, A. Holland, K. Holland, D. Burt, H. Murao, T. Hatsui, *Rev. Sci. Instrum.* **2014**, *85*, 033110.
[53] T. Nakane, Y. Joti, K. Tono, M. Yabashi, E. Nango, S. Iwata, R. Ishitani, O. Nureki, *J. Appl. Crystallogr.* **2016**, *49*, 1035.
[54] T. A. White, R. A. Kirian, A. V. Martin, A. Aquila, K. Nass, A. Barty, H. N. Chapman, *J. Appl. Crystallogr.* **2012**, *45*, 335.
[55] A. Barty, R. A. Kirian, F. R. N. C. Maia, M. Hantke, C. H. Yoon, T. A. White, H. Chapman, *J. Appl. Crystallogr.* **2014**, *47*, 1118.
[56] T. A. White, V. Mariani, W. Brehm, O. Yefanov, A. Barty, K. R. Beyerlein, F. Chervinskii, L. Galli, C. Gati, T. Nakane, A. Tolstikova, K. Yamashita, C. H. Yoon, K. Diederichs, H. N. Chapman, *J. Appl. Crystallogr.* **2016**, *49*, 680.
[57] A. J. Mccoy, R. W. Grosse-Kunstleve, P. D. Adams, M. D. Winn, L. C. Storoni, R. J. Read, *J. Appl. Crystallogr.* **2007**, *40*, 658.
[58] P. D. Adams, P. V. Afonine, G. Bunkóczi, V. B. Chen, I. W. Davis, N. Echols, J. J. Headd, L.-W. Hung, G. J. Kapral, R. W. Grosse-Kunstleve, A. J. Mccoy, N. W. Moriarty, R. Oeffner, R. J. Read, D. C. Richardson, J. S. Richardson, T. C. Terwilliger, P. H. Zwart, *Acta Crystallogr. Sect. D Biol. Crystallogr.* **2010**, *66*, 213.
[59] P. Emsley, B. Lohkamp, W. G. Scott, K. Cowtan, *Acta Crystallogr. Sect. D Biol. Crystallogr.* **2010**, *66*, 486.
[60] W. L. Delano, *The PyMOL Molecular Graphics System. CCP4 Newsl., Protein Crystallogr.* **2002**.
[61] A. M. Waterhouse, J. B. Procter, D. M. A. Martin, M. Clamp, G. J. Barton, *Bioinformatics* **2009**, *25*, 1189.
[62] MathWorks, *T. MATLAB (R2020b)*, MathWorks Inc. **2020**.
[63] J. C. Phillips, R. Braun, W. Wang, J. Gumbart, E. Tajkhorshid, E. Villa, C. Chipot, R. D. Skeel, L. Kalé, K. Schulten, *J. Comput. Chem.* **2005**, *26*, 1781.
[64] J. Huang, S. Rauscher, G. Nawrocki, T. Ran, M. Feig, B. L. De Groot, H. Grubmüller, A. D. Mackerell, *Nat. Methods.* **2017**, *14*, 71.
[65] S. Jo, T. Kim, V. G. Iyer, W. Im, *J. Comput. Chem.* **2008**, *29*, 1859.
[66] T. J. Dolinsky, J. E. Nielsen, J. A. Mccammon, N. A. Baker, *Nucleic Acids Res.* **2004**, *32*, W665.
[67] J. A. White, F. L. Román, A. González, S. Velasco, *Phys. A Stat. Mech. its Appl.* **2008**, *387*, 6705.
[68] A. Y. Toukmaji, J. A. Board, *Comput. Phys. Commun.* **1996**, *95*, 73.
[69] Q. Li, X. Peng, T. Peng, Q. Tang, C. Liu, X. Shi, *J. Comput. Theor. Nanosci.* **2016**, *13*, 4629.
[70] D. Macuglia, *Arch. Hist. Exact Sci.* **2023**, *77*, 345.
[71] W. Humphrey, A. Dalke, K. Schulten, *J. Mol. Graph.* **1996**, *14*, 33.

© 2025 The Author(s). Small Structures published by Wiley-VCH GmbH

26884062, 2025, 8, Downloaded from https://onlinelibrary.wiley.com/doi/10.1002/sstr.202400680 by Koc University, Wiley Online Library on [19/08/2025]. See the Terms and Conditions (https://onlinelibrary.wiley.com/terms-and-conditions) on Wiley Online Library for rules of use; OA articles are governed by the applicable Creative Commons License